



Cite this: *Phys. Chem. Chem. Phys.*,  
2015, 17, 16418

# Graphene allotropes under extreme uniaxial strain: an *ab initio* theoretical study†

Zacharias G. Fthenakis\*<sup>ab</sup> and Nektarios N. Lathiotakis\*<sup>cd</sup>

Using density functional theory calculations, we study the response of three representative graphene allotropes (two pentaheptites and octagraphene) as well as graphene, to uniaxial strain up to their fracture limit. Those allotropes can be seen as distorted graphene structures formed upon periodically arranged Stone–Wales transformations. We calculate their mechanical properties (Young's modulus, Poisson's ratio, speed of sound, ultimate tensile strength and the corresponding strain), and we describe the pathways of their fracture. Finally, we study strain as a factor for the conversion of graphene into those allotropes upon Stone–Wales transformations. For specific sets of Stone–Wales transformations leading to an allotrope, we determine the strain directions and the corresponding minimum strain value, for which the allotrope is more favorable energetically than graphene. We find that the minimum strain values which favor those conversions are of the order of 9–13%. Moreover, we find that the energy barriers for the Stone–Wales transformations decrease dramatically under strain, however, they remain prohibitive for structural transitions. Thus, strain alone cannot provide a synthetic route to these allotropes, but could be a part of composite procedures for this purpose.

Received 24th April 2015,  
Accepted 26th May 2015

DOI: 10.1039/c5cp02412a

www.rsc.org/pccp

## 1 Introduction

The rise of graphene, which followed its isolation and identification,<sup>1</sup> has inevitably fueled the interest in alternative two dimensional materials, like boron nitride,<sup>2,3</sup> metallic dichalcogenides,<sup>4</sup> graphene allotropes<sup>5</sup> (*i.e.* entirely planar three-fold coordinated carbon structures), *etc.* Theoretically, several graphene allotropes have been predicted to be stable.<sup>6–10</sup> A class of them, known as “haeckelites”,<sup>6,8–10</sup> can be derived from graphene upon extensive periodically arranged Stone–Wales transformations‡ (SWTs).<sup>11,12</sup>

Theoretical investigations on haeckelites were started in the mid-1990s by Crespi *et al.*,<sup>6</sup> who proposed and studied the electronic properties of a pentaheptite structure (*i.e.* a haeckelite built entirely out of pentagonal and heptagonal carbon rings),

finding that it is planar, metallic and at least as stable as C<sub>60</sub>. A few years later, Terrones *et al.*,<sup>10</sup> who introduced the term “haeckelites”, studied the stability and electronic, mechanical and vibrational properties of three such structures and their nanotube counterparts.<sup>10,13</sup> Another haeckelite, which has received attention recently<sup>5,14–19</sup> is the so-called octagraphene<sup>14</sup> (OcGr) or T-graphene,<sup>15</sup> which is built entirely of square and octagonal carbon rings. Apparently, there is a whole world of complex planar-sp<sup>2</sup> carbon allotropes consisting partially of hexagons and/or pairs of heptagons–pentagons and/or squares–octagons. In the last decade, the properties of these,<sup>20–22</sup> as well as several other similar periodic,<sup>9,23–26</sup> and amorphous<sup>27</sup> haeckelite structures, have been investigated. Haeckelites could have unique and maybe tailored properties of technological interest. For instance, they can be either metallic or not,<sup>23</sup> or they can be planar or buckled, depending on the arrangement of the SWTs.§

Despite the theoretical predictions for their stability, periodic haeckelite structures have not been synthesized yet. On the other hand, haeckelite-like motifs and line defects based on SWTs or similar transformations have been observed locally in graphene and/or synthesized experimentally. Such structures include graphene with point SW defects,<sup>29</sup> amorphous haeckelite structures,<sup>27,30</sup> haeckelite-like 5–7 or 5–8 line defects,<sup>31,32</sup> grain boundaries,<sup>33</sup> grain boundary loops of pentagons and heptagons<sup>34</sup> and reconstructed graphene edges of alternating pentagonal and heptagonal carbon rings.<sup>35</sup> This fact indicates that

<sup>a</sup> Physics and Astronomy Department, Michigan State University, East Lansing, Michigan 48824, USA

<sup>b</sup> Institute of Electronic Structure and Laser, FORTH, P.O. Box 1527, 71110 Heraklio, Crete, Greece. E-mail: fthenak@iesl.forth.gr

<sup>c</sup> Theoretical and Physical Chemistry Institute, National Hellenic Research Foundation, Vass. Constantinou 48, GR-11635 Athens, Greece. E-mail: lathiot@eie.gr

<sup>d</sup> Max-Planck-Institut für Mikrostrukturphysik, Weinberg 2, D-06120 Halle (Saale), Germany

† Electronic supplementary information (ESI) available. See DOI: 10.1039/c5cp02412a

‡ A SWT is the rotation of a bond around its center by 90°, which results in the conversion of a pyrene unit (composed of four hexagons, which are adjacent to the rotated bond), to two pentagons and two heptagons.

§ An isolated SW defect results in local buckling of graphene.<sup>7,28</sup>

periodic haeckelite structures could be synthesized in the future. It is also worth mentioning the reknitting process,<sup>36</sup> which spontaneously takes place in graphene nanoholes, by filling up with non-hexagonal carbon rings.

Among the possible haeckelite synthetic routes,<sup>6,26</sup> the direct one, by rotating appropriate C–C bonds of the graphene lattice, seems to be prohibitive, since there is a huge energy barrier for this process. According to Crespi *et al.*,<sup>6</sup> this barrier is of the order of 7 eV attributed to the breaking of two C–C bonds along the rotation pathway. An even higher value of 9.2 eV has also been reported.<sup>37</sup> On the other hand, this barrier has been shown theoretically to reduce substantially through catalytic paths in the presence of external atoms,<sup>38</sup> using boron doping,<sup>39</sup> or upon strain, as reported by Samsonidze *et al.*<sup>40</sup> using an atomistic model.

Although most of the theoretical studies on haeckelites focus on their stability and electronic properties, little has been done on their response to stress.<sup>7,14,41,42</sup> In the present work, we attempt to cover this gap. Experimentally, large uniaxial stress, up to the fracture limit, has been applied to a graphene monolayer,<sup>43</sup> measuring its ultimate tensile strength (UTS) and the corresponding strain  $\varepsilon = 0.25$ . Of course, a relevant question is whether graphene remains energetically more stable than its planar allotropes in the regime of so large uniaxial deformation. In the present work, we also attempt to answer this question.

More specifically, we consider two periodic pentaheptite structures, which we call PeHe-A and PeHe-B (see Fig. 1(c), top and bottom panels, respectively) and OcGr (Fig. 1(f) top and bottom) and we study their mechanical properties for uniaxial stretching in comparison with graphene, up to the fracture limits, using *ab initio* density functional theory (DFT) calculations.

We plot their stress–strain curves and calculate their Young's modulus, Poisson's ratio, speed of sound, and ultimate stress–strain limits for different strain directions. Additionally, we examine if strain can be an assisting factor for their synthesis. In particular, we determine the strain directions and corresponding strain values that favor the relative energy stability of the SWTs leading to the allotropes. For this purpose, we use both a harmonic approximation and DFT calculations and check for the existence of crossing points in the plots of the total energies as a function of strain along these directions. Finally, using a prototype molecular system, we estimate the energy barrier for SWTs as a function of strain.

The present paper is organized as follows: In Section 2, we describe the structures we considered and the periodic SWTs that lead to them, as well as our methodology. In Section 3, we present and discuss our results on the equilibrium and mechanical properties of the allotropes (Section 3.1), their UTS and fracture patterns (Section 3.2), and finally their relative stability as a function of uniaxial strain (Section 3.3). The conclusions are included in Section 4.

## 2 Structures and methods

In Fig. 1(a)–(c), we show the mechanism of conversion of graphene into PeHe-A and PeHe-B (top and bottom panels, respectively) through periodic arrangements of SWTs. The bonds in graphene (a) colored in red have been rotated by 90° as shown in (b) and the relaxed PeHe-A and PeHe-B structures are shown in (c). We note that PeHe-B is the pentaheptite structure introduced by Crespi *et al.*<sup>6</sup> Furthermore, in Fig. 1(d)–(f), we show the

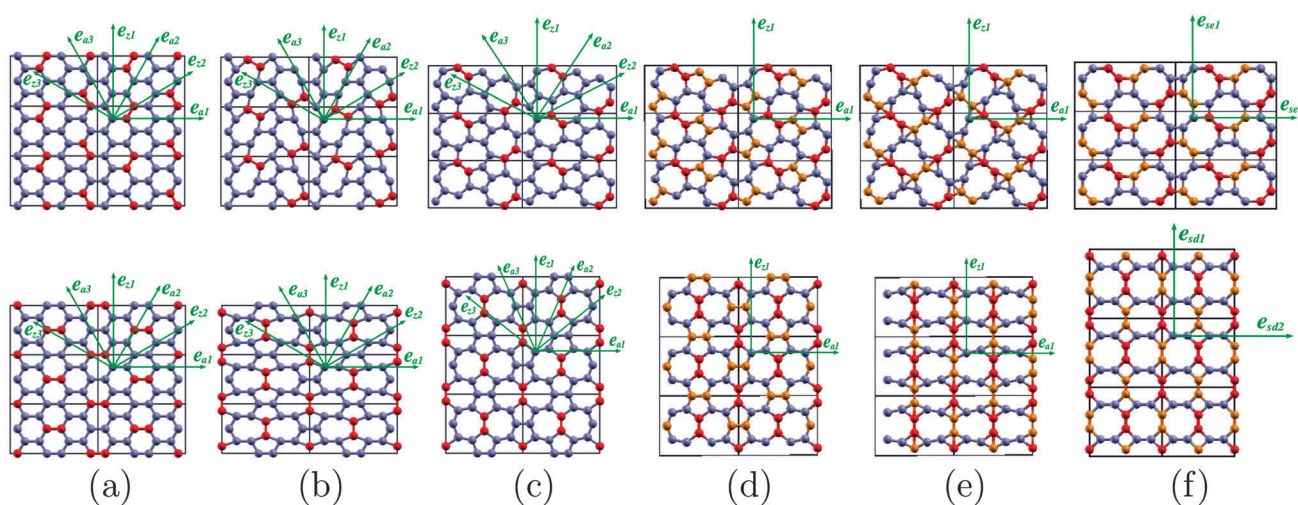


**Fig. 1** Representative structure conversions through periodic meshes of SWTs: conversion of graphene into PeHe-A ( $G \rightarrow A$ ) and PeHe-B ( $G \rightarrow B$ ) in top and bottom (a)–(c) panels, respectively, and further the conversion of PeHe-A ( $A \rightarrow O$ ) and PeHe-B ( $B \rightarrow O$ ) into OcGr in top and bottom (d)–(f), respectively. In (a), graphene and the mesh of rotating bonds (in red) are shown; in (b), 90° bond rotations have been performed in the otherwise unperturbed lattice; in (c), the optimized PeHe-A (top) and PeHe-B (bottom) structures are shown; in (d), PeHe-A and PeHe-B structures are shown, with the additional rotating bonds (in orange) leading, in both cases, to OcGr; in (e), 90° rotations have been performed in the otherwise unperturbed lattices; in (f), the optimized OcGr structures are shown. The rotation of the red colored bonds in (a) together with the orange in (d) constitute the two different sets of SWTs that convert graphene into OcGr, labeled  $(G \xrightarrow{A} O)$  and  $(G \xrightarrow{B} O)$  (top and bottom panels, respectively). The green arrows show the considered strain directions.

conversion mechanism of PeHe-A and PeHe-B (top and bottom panels, respectively) to OcGr. The rotation by  $90^\circ$  of all the common bonds of adjacent pentagons (colored in orange) in either PeHe-A ((d) (top)) or PeHe-B ((d) (bottom)), lead to the structures in (e) which upon optimization relax to OcGr in (f). The structures in the top and bottom panels in (f) are identical but rotated with respect to each other by  $45^\circ$ .

Due to the symmetry reduction associated with the arrangement of SWTs, the primitive unit cells in PeHe-A, PeHe-B and OcGr contain 16, 8 and 4 atoms, respectively. For the purpose of the present study, we adopt a common rectangular 16-atom unit cell, shown with black lines in Fig. 1.

In order to investigate the response of the structures under study to strain, we optimize them under constant strain along certain representative high symmetry directions. For graphene, PeHe-A and PeHe-B these directions are defined in terms of fractional coordinates, with respect to the selected rectangular unit cell vectors: (0,1), (1,1), (-1,1), (1,0), (1,3) and (-1,3). They are shown in Fig. 1(a-c) denoted as  $e_{z1}$ ,  $e_{z2}$ ,  $e_{z3}$ ,  $e_{a1}$ ,  $e_{a2}$ ,  $e_{a3}$ , respectively. For graphene, they correspond to the three equivalent directions along zig-zag ( $e_{z1}$ ,  $e_{z2}$  and  $e_{z3}$ ) and the three equivalent directions along arm-chair chains ( $e_{a1}$ ,  $e_{a2}$  and  $e_{a3}$ ) which we will simply call zig-zag and arm-chair directions. Occasionally we will use the notation  $e_a$ ,  $e_z$  referring to them. However, for PeHe-A and PeHe-B, only  $e_{z1}$ ,  $e_{z2}$ ,  $e_{a1}$  and  $e_{a2}$  are different from each other, since under the structural transformations  $x \rightarrow -x + c_x$  and  $y \rightarrow y + c_y$  (for certain constant values of  $c_x$  and  $c_y$ ) for PeHe-A, and  $x \rightarrow -x$  for PeHe-B,  $e_{z3}$  and  $e_{a3}$  coincide with  $e_{z2}$  and  $e_{a2}$ , respectively. In the present study, we focus on the effect of strain in the directions  $e_{a1}$ ,  $e_{z1}$  and  $e_{z2}$  for PeHe-A and  $e_{a1}$ ,  $e_{z1}$ , and  $e_{a2}$  for PeHe-B. In the case of  $e_{z2}$  and  $e_{a2}$ , a non-rectangular unit cell is adopted, as required in order to keep the same number of atoms per unit cell. After the conversion of PeHe-A and PeHe-B to OcGr, shown in Fig. 1(d)-(f), the directions  $e_{a1}$  and  $e_{z1}$  become equivalent in both cases. Thus, to avoid confusion, for OcGr, we adopt the notation  $e_{se}$  (direction along a square edge), and  $e_{sd}$  (along square diameter). In the case of PeHe-A conversion,  $e_{a1}$  and  $e_{z1}$  become  $e_{se1}$ ,  $e_{se2}$ , while for PeHe-B they become  $e_{sd1}$ ,  $e_{sd2}$ , respectively.

For our calculations, we used the Quantum Espresso<sup>44</sup> periodic DFT code at the level of a GGA/PBE functional.<sup>45</sup> We adopted an ultra-soft pseudopotential<sup>46</sup> for C, generated by a modified RRKJ approach.<sup>47</sup> We used k-meshes of the order of  $6 \times 12$  points which were found sufficient to converge structural properties given the relatively large size of the adopted unit-cell. We chose cutoffs 50 and 500 Ryd for the wave functions and charge density, respectively, and occupation smearing of 5 mRyd. Calculations under constant strain were performed by scaling and freezing the corresponding unit-cell vector while all the rest of the structural parameters, *i.e.* atom positions and cell dimensions, were fully optimized.

## 3 Results and discussion

### 3.1 Structural and mechanical properties

According to our findings, the optimized PeHe-A and PeHe-B structures are by 0.22 and 0.24 eV per atom, respectively,

less favorable than graphene. The optimized OcGr structure is by 0.25 eV per atom higher than PeHe-B. These energy differences correspond to an energy cost of  $\approx 1.8$ – $2.0$  eV per single SWT.

As seen in Fig. 1(c), the lattice of PeHe-A and PeHe-B remains rectangular upon optimization. However, the lattice parameter of PeHe-A in the  $e_{a1}$  direction increases while that of the  $e_{z1}$  decreases. In the case of PeHe-B, we have the opposite, *i.e.* the lattice parameter increases along the  $e_{z1}$  direction and decreases along the  $e_{a1}$ . For PeHe-B, this change in dimensions looks plausible since the structure is enlarged in the direction that the bonds turn to, as a stress reduction mechanism. For PeHe-A, a similar mechanism takes place although the bonds are never parallel to any of the lattice vectors. Similarly, however, enlargement of the structure occurs in the direction with the largest projection of the rotated bonds. The magnitude of the lattice vectors for the rectangular lattice of PeHe-A and PeHe-B, shown in Fig. 1, are  $a_x = 9.157$  Å and  $a_y = 4.749$  Å for PeHe-A, and  $a_x = 7.460$  Å and  $a_y = 5.847$  Å for PeHe-B, respectively. The magnitude of the corresponding lattice vectors for graphene is  $a_{g,x} = 6a_0 = 8.531$  Å and  $a_{g,y} = 2\sqrt{3}a_0 = 4.925$  Å, where  $a_0 = 1.422$  Å is the bond length. For the square lattice of OcGr, the lattice constant  $a$  is  $a = 2(a_1 + \sqrt{2}a_2) = 6.877$  Å, where  $a_1 = 1.370$  Å and  $a_2 = 1.462$  Å are the bond lengths corresponding to the adjacent octagon edges and the square edges, respectively.

We calculate the response of PeHe-A, PeHe-B and OcGr as well as graphene for uniaxial stress  $\sigma$ , for strains  $\varepsilon$  ranging from  $-20\%$  up to  $30\%$ . As it is customary, to obtain values relevant for comparison with 3-dimensional materials<sup>43,48</sup> we consider a structure thickness of  $3.34$  Å (the interlayer separation distance of graphite).

Obviously, any 2-dimensional (2D) structure under compression would prefer to bend instead of remaining flat and negatively strained.<sup>51</sup> However, it is possible to perform calculations for negative strains, without structure bending, in order to estimate, more reliably, quantities that are expressed as derivatives  $dA/d\varepsilon$ , or as ratios  $A/\varepsilon$ , at  $\varepsilon = 0$ , using least square fitting, rather than extrapolating positive strain results to  $\varepsilon = 0$ . Such quantities are Young's modulus  $E$ , ( $E = \sigma/\varepsilon$ ), and Poisson's ratio  $\nu$  ( $\nu = -\varepsilon_\perp/\varepsilon$ , where  $\varepsilon_\perp$  is the transverse strain).

In Fig. 2(a), we show the stress-strain curves for all structures in the range  $0 \leq \varepsilon \leq 0.3$ . In agreement with other theoretical<sup>48–50,52,53</sup> and experimental<sup>43</sup> studies in graphene, we find a non-linear stress-strain relation not only for graphene, but also for the allotropes of our study, even for stress less than 5%. For graphene, it has been proposed<sup>43</sup> that this non-linear behavior can be expressed as  $\sigma = E\varepsilon + D\varepsilon^2$  (which is equivalent to a linear dependence of  $\sigma/\varepsilon$  on  $\varepsilon$ ), although an even higher order expansion in strain has been considered.<sup>49</sup> However, as shown in Fig. S1(c) of the ESI,<sup>†</sup> the dependence of  $\sigma/\varepsilon$  on  $\varepsilon$  diverges from linearity for the strain range we considered and for all the structures. We found a more accurate description fitting to the quadratic equation

$$\sigma/\varepsilon = E + D\varepsilon + F\varepsilon^2, \quad (1)$$

for  $0 < \varepsilon \lesssim \varepsilon_u$ , where  $\varepsilon_u$  is the strain corresponding to the UTS. The fitting lines are presented in Fig. 2(a) and Fig. S1(c) of

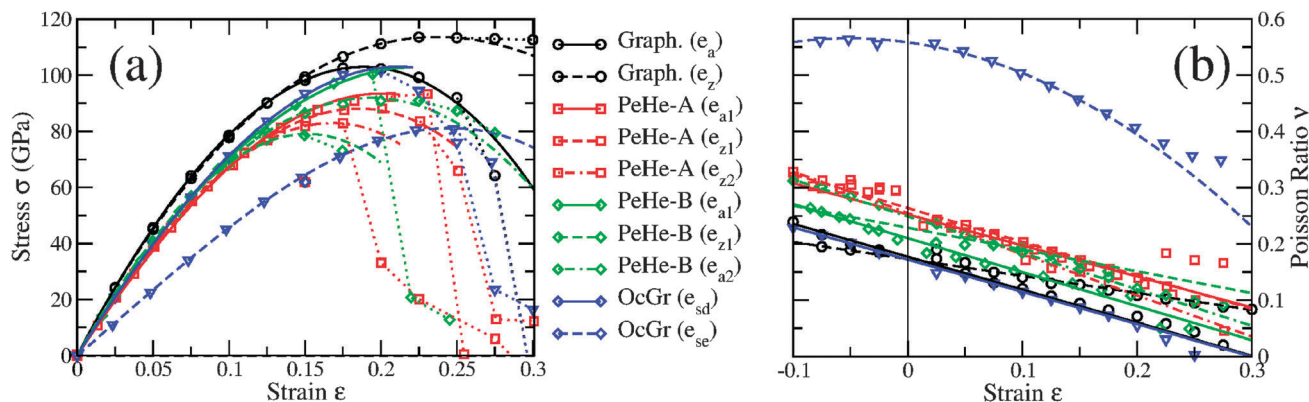


Fig. 2 (a) Stress–strain curves and (b) Poisson's ratios as a function of strain, for graphene, PeHe-A, PeHe-B, and OcGr for different strain directions. The straight, dashed and dot-dashed lines in the stress–strain graph are the fitting lines according to eqn (1) and (2) for (a) and (b), respectively. The dotted lines in (a) connect the stress–strain points for strain values  $\varepsilon \approx \varepsilon_u$ .

the ESI.<sup>†</sup> However,  $D$  and  $F$  depend strongly on the range of  $\varepsilon$  and the degree of the fitting polynomial used in the fitting method, indicating that even a fitting using eqn (1) cannot provide reliable values for  $D$  and  $F$  (see ESI,<sup>†</sup> for more details).

Young's moduli  $E$  have been estimated by fitting a 3rd degree polynomial of the form  $\sigma = Fe^3 + De^2 + Ee$  to the  $(\varepsilon, \sigma)$  values for  $\varepsilon$  in the range of  $-0.1 \leq \varepsilon \leq 0.1$  (ESI,<sup>†</sup> Fig. S1(a)). For Poisson's ratio  $\nu$  at ambient strain we fitted a quadratic equation of the form

$$\varepsilon_{\perp} = \nu_1 \varepsilon^2 - \nu \varepsilon \quad (2)$$

to the  $(\varepsilon, \varepsilon_{\perp})$  values for the same  $\varepsilon$  range (Fig. S1(b) of the ESI<sup>†</sup>). The obtained values of Young's modulus and Poisson's ratio are presented in Table 1 together with other theoretical and experimental values.

As we see in Fig. 2 and Table 1, all structures appear to be quite isotropic in terms of stiffness and Poisson's ratio with OcGr being a striking exception. As expected, graphene exhibits isotropic behavior along  $e_a$  and  $e_z$  directions, with the highest  $E$  value among all structures. The anisotropy for graphene of  $\approx 0.2\%$  and  $\approx 1\%$  on the average for Young's modulus and Poisson's ratio, respectively, can be attributed to numerical errors. The anisotropy of PeHe-A and PeHe-B is  $\approx 5\text{--}6\%$  for stiffness, while for Poisson's ratio it is  $\approx 5\%$  and  $\approx 20\%$  for PeHe-A and PeHe-B, respectively.

The structures under investigation can be sorted in terms of stiffness, from the highest to the lowest  $E$  values as: graphene  $>$  PeHe-B  $>$  OcGr( $e_{sd}$ )  $\approx$  PeHe-A  $>$  OcGr( $e_{se}$ ). In terms of Poisson's ratio from the lowest to the highest  $\nu$  they

Table 1 Calculated Young's modulus  $E$ , Poisson's ratio  $\nu$ , mass density  $\rho$ , speed of sound  $v_s$ , UTS  $\sigma_u$  and the corresponding strain values  $\varepsilon_u$  in different directions for graphene, PeHe-A, PeHe-B and OcGr compared with other values reported. Values in parentheses are not provided in, but evaluated using data from, the corresponding publication

| Structure | Source/method           | Direction  | $E$ (GPa)  | $\nu$ | $\rho$ (gr cm <sup>-3</sup> ) | $v_s$ (km s <sup>-1</sup> ) | $\varepsilon_u$ | $\sigma_u$ (GPa) |
|-----------|-------------------------|------------|------------|-------|-------------------------------|-----------------------------|-----------------|------------------|
| Graphene  | Present work            | $e_a$      | 1024       | 0.177 | 2.291                         | 21.14                       | 0.185           | 103              |
|           | Present work            | $e_z$      | 1020       | 0.173 | 2.291                         | 21.10                       | 0.225           | 114              |
|           | LDA <sup>42</sup>       | $e_a, e_z$ | 1054       | 0.185 | (2.314)                       | (21.34)                     |                 |                  |
|           | LDA <sup>48</sup>       | $e_a, e_z$ | 1050       | 0.186 | (2.313)                       | (21.30)                     | 0.194           | 110, 121         |
|           | GGA/PBE <sup>49</sup>   | $e_a, e_z$ | 1042       | 0.169 | (2.323)                       | (21.18)                     |                 | 118              |
|           | GGA/PBE <sup>42</sup>   | $e_a, e_z$ | 1025       | 0.173 | (2.277)                       | (21.22)                     |                 |                  |
|           | GGA/PW <sup>14</sup>    | $e_a, e_z$ | 1048       | 0.17  | (2.305)                       | (21.32)                     |                 | 104, 115         |
|           | Atomistic <sup>50</sup> | $e_a, e_z$ | 960        | 0.22  | (2.29)                        | (20.47)                     |                 | 100, 120–130     |
|           | Exp. <sup>43</sup>      |            | 1020 ± 150 |       |                               |                             | 0.25            | 126 ± 12         |
| PeHe-A    | Present work            | $e_{a1}$   | 825        | 0.253 | 2.213                         | 19.3                        | 0.240           | 94               |
|           | Present work            | $e_{z1}$   | 860        | 0.264 | 2.213                         | 19.7                        | 0.192           | 88               |
|           | Present work            | $e_{z2}$   | 865        | 0.255 | 2.213                         | 19.8                        | 0.169           | 83               |
| PeHe-B    | Present work            | $e_{a1}$   | 882        | 0.210 | 2.207                         | 20.0                        | 0.201           | 101              |
|           | Present work            | $e_{z1}$   | 937        | 0.229 | 2.207                         | 20.6                        | 0.144           | 79               |
|           | Present work            | $e_{a2}$   | 897        | 0.249 | 2.207                         | 20.2                        | 0.214           | 91               |
|           | GGA/PBE <sup>42</sup>   | $e_{a1}$   | 885        | 0.208 | (2.196)                       | (20.1)                      |                 |                  |
|           | GGA/PBE <sup>42</sup>   | $e_{z1}$   | 929        | 0.218 | (2.196)                       | (20.6)                      |                 |                  |
| OcGr      | Present work            | $e_{sd}$   | 866        | 0.172 | 2.035                         | 20.6                        | 0.193           | 102              |
|           | Present work            | $e_{se}$   | 461        | 0.558 | 2.035                         | 15.1                        | 0.238           | 82               |
|           | GGA/PBE <sup>42</sup>   | $e_{sd}$   | 854        | 0.185 | (2.021)                       | (20.6)                      |                 |                  |
|           | GGA/PW <sup>14</sup>    | $e_{sd}$   | 916        | 0.13  | 2.036                         | (21.2)                      |                 | 103              |
|           | GGA/PW <sup>14</sup>    | $e_{se}$   | 503        | 0.47  | 2.036                         | (15.7)                      |                 | 82               |

can be sorted as: OcGr( $e_{sd}$ )  $\approx$  graphene < PeHe-B < PeHe-A < OcGr ( $e_{se}$ ). The highly anisotropic behavior of OcGr has been studied and explained in detail elsewhere,<sup>54</sup> and it has been attributed to the topology of OcGr.

Using the obtained values for  $E$ , we can calculate the longitudinal speed of sound  $v_s = \sqrt{E/\rho}$  ( $\rho$  is the mass density), for the corresponding direction. The values of  $v_s$  for all the structures and the strain directions we considered are presented in Table 1. As one can see, graphene exhibits the highest  $v_s$  value. Excluding OcGr in the  $e_{se}$  direction, all allotropes (including graphene) exhibit high  $v_s$  values, ranging between 19.3 and 21.14 km s<sup>-1</sup>. Similar  $v_s$  values have been reported for PeHe-A, PeHe-B and graphene (19.7, 20.0 and 24.0 km s<sup>-1</sup>, respectively)<sup>22</sup> using the slope at  $\Gamma$  point of the phonon dispersion obtained with the use of the Tersoff interatomic potential.

### 3.2 Ultimate tensile strength and fracture

We estimate the UTS,  $\sigma_u$ , corresponding to an ultimate strain  $\epsilon_u$ , by fitting a quadratic function for the stress-strain curve in the region of the highest strain values. Our results are presented in Fig. 3, as well as in Table 1, together with the results from the literature. The half of strain step  $\delta\epsilon/2 = 0.0125$  adopted in our calculations can be considered as the estimated error for  $\epsilon_u$ . For all the structures and strain directions,  $\sigma_u$  is extremely high in comparison with that of common high-UTS materials and are comparable to those of graphene, which exhibit the highest  $\sigma_u$  for both  $e_z$  and  $e_a$  strain directions.

The behavior of OcGr, PeHe-A and PeHe-B under strain in different directions is shown in Fig. 4–8. The series of snapshots in these figures show the structural changes for increasing  $\epsilon$ . In each successive snapshot, at least one additional bond exceeds in length by 1.65 Å, assuming that breaking starts at this value. Bonds that are candidates for breaking are those with the highest elongation. Naturally, such bonds are those which are either directed along or with a small angle to the strain direction. The best examples are bonds in graphene and OcGr. Indeed, for OcGr, the bonds that break are those corresponding to the adjacent octagon edges (for stress along the  $e_{sd}$  direction), or the square edges (for strain along the  $e_{se}$  direction), as shown in Fig. 4. For the  $e_{sd}$  and  $e_{se}$  strain directions and for  $\epsilon > \epsilon_u$ , OcGr was

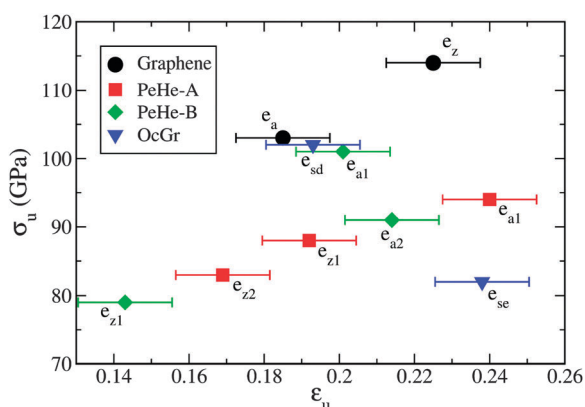


Fig. 3 Ultimate tensile stress  $\sigma_u$  versus  $\epsilon_u$ .

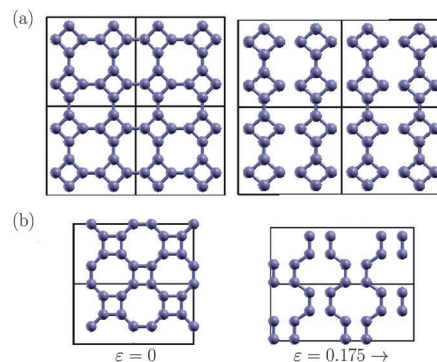


Fig. 4 Snapshots of OcGr for specific strain values along (a)  $e_{sd}$  and (b)  $e_{se}$  directions. Bonds start breaking in both cases at  $\epsilon = 0.175$ . The arrows next to the strain values indicate the strain direction.

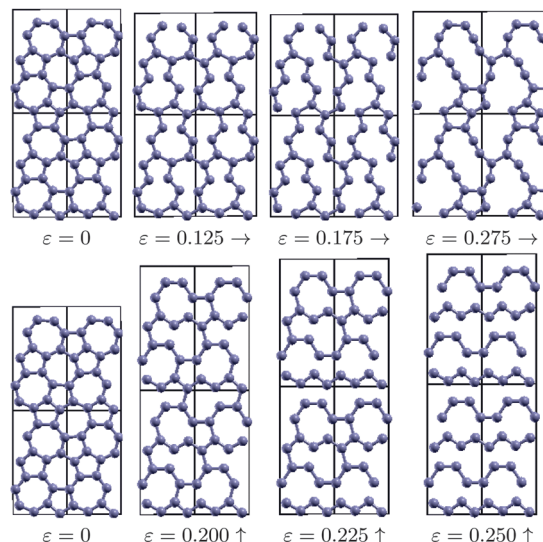


Fig. 5 Snapshots of PeHe-A for specific strains along  $e_{z1}$  (top) and  $e_{a1}$  (bottom). The arrows show the strain direction.

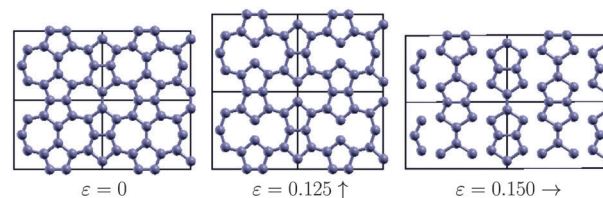


Fig. 6 Snapshots of PeHe-B for specific strains along  $e_{z1}$  (center) and  $e_{a1}$  (right). The arrows show the strain direction.

found to break into lines of interconnected squares or arm-chair chains. For even higher  $\epsilon$  along  $e_{se}$ , e.g.  $\epsilon \approx 0.275$ , straight carbyne chains are obtained.

For graphene strained along the  $e_a$  direction, the bonds are either at an angle of  $\pm 60^\circ$  with respect to the strain direction, or they are parallel to the strain direction. It is expected therefore, that the latter will break first, creating (theoretically) zig-zag chains. On the other hand, for graphene strained along the  $e_z$  direction, the bonds are either at an angle of  $30^\circ$  or vertical to

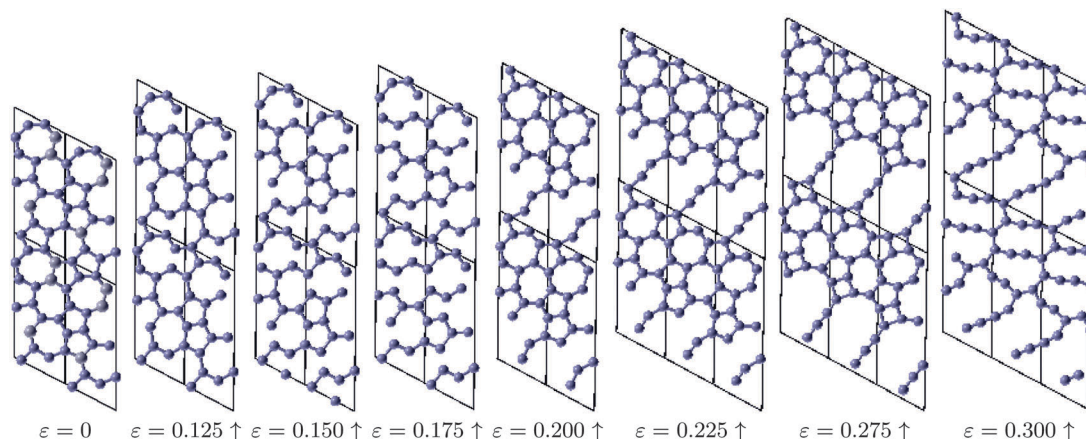


Fig. 7 Snapshots of PeHe-A for specific strain values along  $e_{22}$ . The arrows show the strain direction.

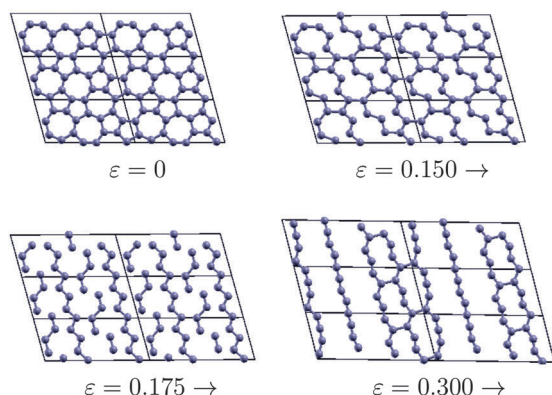


Fig. 8 Snapshots of PeHe-B for strains along  $e_{a2}$ . The arrows show the strain direction.

the strain direction. Therefore, bonds in the zig-zag chains will break first, leading (theoretically) to carbon dimers. In reality, however, more complicated structures will be the products of fracture since not all bonds will break simultaneously. In the fracture processes of graphene, described above, one bond per atom breaks for strain along the  $e_z$  direction, while half a bond per atom breaks for strain along the  $e_a$  direction. This explains why UTS for the  $e_z$  direction is higher than that for the  $e_a$ , as seen in Fig. 3 and Table 1. The theoretically obtained fracture strain for both directions is higher than the maximum value of 0.3, of our study. It is also much higher than the experimental value, due to effects owing to the finite size of the supercell, temperature and defects.

Under extreme strain, *i.e.* for values higher than  $\epsilon_{u1}$ , the investigated allotropes either dissociate into linear chains, or undergo a transition to structures containing carbyne units accompanied by bond recreation, like PeHe-A strained along  $e_{z1}$  and  $e_{z2}$  directions, and PeHe-B strained along the  $e_{a2}$  direction. Those chains are either zig-zag or arm-chair chains (graphene  $e_a$ , OcGr  $e_{se}$ , PeHe-A  $e_{a1}$ , PeHe-B  $e_{a2}$ ), or they are composed of interconnected squares (OcGr  $e_{sd}$ ), or couple of adjacent pentagons (PeHe-B  $e_{a1}$ ). For even higher strain values, arm-chair and zig-zag chains undergo a transition to carbyne chains. As in the

case of graphene, and for similar reasons, the experimental procedure of fracture is expected to be rather more complicated with diverse products and differences in break points.

### 3.3 Strain as a synthetic route factor

As we have seen, at equilibrium, PeHe-A, PeHe-B and OcGr are energetically less stable than graphene while the energy barrier for a SWT is of the order of  $\approx 7$  eV. In this section, we examine how tensile strain influences those two factors for the conversion of graphene to the allotropes of our study. In particular we examine (i) whether there exist strain directions that above a strain value the SWTs leading to the graphene allotropes are energetically favorable and (ii) if the energy barrier for a SWT decreases under strain. Obviously, there is an infinite number of haeckelites and corresponding structural conversions based on SWTs. In this work, we study only a few representative ones, namely the conversions  $G \rightarrow A$ ,  $G \rightarrow B$ ,  $A \rightarrow O$ ,  $B \rightarrow O$ ,  $G \xrightarrow{A} O$ ,  $G \xrightarrow{B} O$ , defined in Fig. 1.

In a possible mechanism for the structural conversions, the initial structure, *e.g.* graphene, can be stretched along a direction favoring energetically SWTs. Then a trigger (possibly consisting of thermalization, catalysis, and/or irradiation) performs specific SWTs which lead to the final structure, *e.g.* one of the allotropes. This specificity is a difficult problem and is not the subject of this work. However, it would be useful to know the directions and strain values favoring energy stability since it might be easier for the required specific triggers to be successful when combined with the appropriate strain in those directions.

The hypothesis that the energy cost for a particular conversion vanishes under strain in a given direction ( $n,m$ ) (in fractional coordinates) can be tested by searching for a crossing point in the plot of the total energies of the initial and final structures considered as functions of the lattice parameter on the same direction ( $n,m$ ). Obviously, the strains of the structures at the crossing point must be considerably smaller than fracture strains. The strain value corresponding to a crossing point, which we call crossing strain,  $\epsilon_{cr}$ , is the minimal strain where the final structure is lower in energy than the initial.

$\varepsilon_{cr}$  refers to the initial structure, as the strain of the final structure at the same lattice parameter is different.

Apart from using DFT calculations, the existence of crossing points can be tested analytically with a simple harmonic approximation for the total energy  $U$ . If crossing strains are large, *i.e.* in the non-elastic regime, this model can only serve as a qualitative analysis to identify the directions that this effect occurs. Writing  $U = k\varepsilon^2 + U_0$ , where  $k = EV/2$ ,  $E$  is Young's modulus and  $V$  the atomic volume, and  $U_0$  is the total energy at the equilibrium, and equating the total energies per atom of the initial and final structures at a strained lattice parameter  $a$  along a specific direction  $(n,m)$ , we obtain

$$k_i(a - a_i)^2/a_i^2 = k_f(a - a_f)^2/a_f^2 + \Delta U. \quad (3)$$

The indices  $i$  and  $f$  refer to the initial and the final structures.  $a_i$  and  $a_f$  are the corresponding equilibrium lattice parameters along the direction  $(n,m)$ , *i.e.*  $a_i = (n^2 a_{i,x}^2 + m^2 a_{i,y}^2)^{1/2}$  and  $a_f = (n^2 a_{f,x}^2 + m^2 a_{f,y}^2)^{1/2}$ , where  $a_{i,x}$ ,  $a_{i,y}$  and  $a_{f,x}$ ,  $a_{f,y}$  are the lattice parameters along  $x$  and  $y$  directions.  $\Delta U$  is the total energy difference of these structures at equilibrium. Alternatively, the angle, between the strain direction and  $e_{a1}$ , which we call strain angle,  $\phi$ , can be used instead of indices  $n, m$  ( $\phi = \arctan[(ma_{i,y})/(na_{i,x})]$ ). Note that for given indices  $(n,m)$ , the strain angle differs from one structure to another. Thus, the term strain angle always refers to the initial structure.

Using the obtained values for  $E$ , we obtain  $k_g \approx 28$  eV for graphene and, assuming, for simplicity, that PeHe-A and PeHe-B are isotropic,  $k_A \approx 24$  eV for PeHe-A and  $k_B \approx 26$  eV for PeHe-B. The  $k$  value for OcGr ( $k_O$ ) depends not only on the strain direction, but also on the SWTs involved (more details are given in the ESI†).

Solving eqn (3) with respect to  $a$ , for a particular strain direction  $(n,m)$ , we can find the crossing strain for that direction. In Fig. 9 we show the crossing strain as a function of the strain angle  $\phi$  in the range of  $[0, 90^\circ]$ , for all the cases. The minimal values of the crossing strain, for each of the structural conversions, together with the corresponding strain angles  $\phi_{min}$  are included

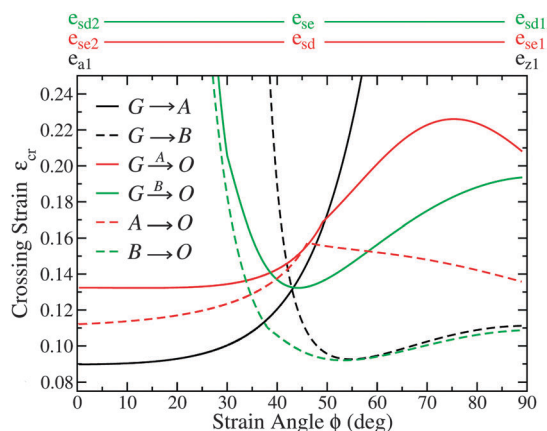


Fig. 9 Dependence of the crossing strain,  $\varepsilon_{cr}$ , on the strain angle,  $\phi$ , for the initial structure, as obtained by the harmonic approximation, for the structural conversions defined in Fig. 1. Strain angles refer to the initial structures.

Table 2 Results of the harmonic approximation on the minimum crossing strain,  $\varepsilon_{min}$ , the corresponding strain angle  $\phi_{min}$ , and the conditions on the indices  $(n,m)$  and strain angles  $\phi$  for the existence of crossing points

| Path                  | $\phi_{min}$ ( $^\circ$ ) | $\varepsilon_{min}$ (%) | $(m,n)$          | $\phi$ ( $^\circ$ ) |
|-----------------------|---------------------------|-------------------------|------------------|---------------------|
| G $\rightarrow$ A     | 0                         | 9                       | $ m  < 2.64 n $  | $ \phi  < 57$       |
| G $\rightarrow$ B     | 55                        | 9                       | $ m  > 1.38 n $  | $38 <  \phi  < 142$ |
| G $\xrightarrow{A}$ O | 13.5                      | 13                      | All              | All                 |
| G $\xrightarrow{B}$ O | 44                        | 13                      | $ m  > 0.967 n $ | $28 <  \phi  < 152$ |
| A $\rightarrow$ O     | 0                         | 11                      | All              | All                 |
| B $\rightarrow$ O     | 53                        | 9                       | $ m  > 0.675 n $ | $27 <  \phi  < 153$ |

in Table 2. As we see, the minimal crossing strains are in the range of 9–13%. These values, however, are expected to be smaller than those obtained from DFT calculations due to anharmonicity at these strains.

Imposing that  $a < 1.25a_i$ , *i.e.* for  $\varepsilon$  smaller than the experimental<sup>43</sup> UTS for graphene, we arrive at the conditions for the existence of crossing points along  $(n,m)$ . These conditions are also shown in Table 2 for the values of  $n, m$  and the strain angle  $\phi$ . As one can see, among the high symmetry strain directions considered in the DFT calculations of this work, only  $e_{a1}$  and  $e_{z2}$  favor the G  $\rightarrow$  A and  $e_{z1}$  and  $e_{a2}$  the G  $\rightarrow$  B, while for the G  $\xrightarrow{A}$  O, G  $\xrightarrow{B}$  O, A  $\rightarrow$  O and B  $\rightarrow$  O, all the considered directions favor the formation of OcGr apart from  $e_{a1}$  in the cases of B  $\rightarrow$  O and G  $\xrightarrow{B}$  O.

The results of the harmonic approximation analysis are confirmed by the results of our DFT calculations, which are shown in Fig. 10. In Fig. 10(a), we show the total energy of graphene, as a function of the lattice parameter along  $e_a$  (*i.e.*  $e_{a1}$ ,  $e_{a2}$  and  $e_{a3}$  equivalent directions for graphene). In the same graph, we show the total energy of PeHe-A strained along  $e_{a1}$ , PeHe-B strained along  $e_{a2}$  and OcGr strained along the  $e_{se}$  direction, as these directions were found by the harmonic approximation to favor G  $\rightarrow$  A, G  $\rightarrow$  B and G  $\xrightarrow{A}$  O, respectively. As one can see, graphene strained along  $e_a$  is energetically more favorable than PeHe-A strained along  $e_{a1}$  and PeHe-B along  $e_{a2}$  until  $1.10 a_{g,x}$ , *i.e.*  $\varepsilon_{cr} \approx 10\%$ . For higher strains, the periodic net of SWTs for the conversions G  $\rightarrow$  A and G  $\rightarrow$  B lead to energy lowering. Apart from a tiny region beyond the crossing point, that PeHe-A is energetically lower, PeHe-B appears to be the optimal for a broad region of the lattice parameter. OcGr strained along the  $e_{se}$  direction becomes energetically more favorable than graphene (G  $\xrightarrow{A}$  O conversion) and PeHe-A (A  $\rightarrow$  O conversion) both strained along the  $e_{a1}$  direction, for  $a > 1.15a_{g,x}$  and  $a > 1.22a_{g,x}$ , respectively, corresponding to  $\varepsilon_{cr} \approx 15\%$  for graphene and 14% for PeHe-A.

Similarly, in Fig. 10(b), we show the DFT results for the total energy of graphene as a function of its lattice parameter, strained along the three equivalent  $e_z$  directions, together with the total energy of PeHe-A strained along  $e_{z2}$ , PeHe-B strained along  $e_{z1}$ , and OcGr strained along both  $e_{se}$  and  $e_{sd}$  directions, since these directions were found by the harmonic approximation to favour G  $\rightarrow$  A, G  $\rightarrow$  B, G  $\xrightarrow{A}$  O and G  $\xrightarrow{B}$  O conversions, respectively. As one can see, graphene strained along the  $e_z$  direction is

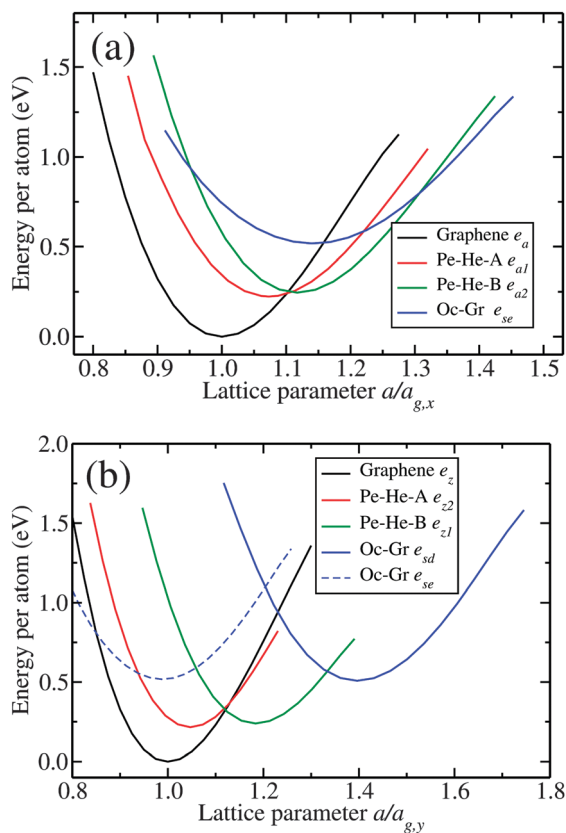


Fig. 10 Total energy per atom, obtained with DFT calculations, versus lattice parameters for the zig-zag and armchair directions, respectively.

energetically less favorable than PeHe-A strained along  $e_{z2}$ , PeHe-B along  $e_{z1}$  and OcGr along the  $e_{sd}$  direction, for  $a > 1.12a_{g,y}$ ,  $1.13a_{g,y}$  and  $1.23a_{g,y}$ , respectively (*i.e.* for  $\varepsilon > 12\%$ ,  $13\%$  and  $23\%$ , respectively). These strain values are larger than the corresponding values for the arm-chair directions for these structures. Moreover, PeHe-B strained along the  $e_{z1}$  direction is less favorable than OcGr along  $e_{sd}$  for  $a > 1.33a_{g,y}$ , corresponding to strain  $\varepsilon = 12\%$  for PeHe-B. As seen, the energetically most favorable structure for  $1.12a_{g,y} < a < 1.33a_{g,y}$  is PeHe-B strained along the  $e_{z1}$  direction, while for  $a > 1.33a_{g,y}$ , the most favorable is OcGr strained along  $e_{sd}$ .

As expected, the crossing points obtained by the harmonic approximation analysis are lower by 10–23% compared with the DFT results. In addition, in contrast to the prediction of the harmonic approximation, Fig. 10(b) shows that there is no crossing point of the energy curves of graphene strained along  $e_{z1}$  and OcGr strained along  $e_{se}$  directions. According to the harmonic approximation prediction, there is a crossing point at graphene strain  $\varepsilon \approx 21\%$ . Such discrepancies are due to the anharmonicity present at large strains. Graphene is softening in that regime, as shown in Fig. 2(a), resulting in a bending of the total energy curve towards larger strain values. This bending explains both the larger values of crossing strains obtained by DFT calculations compared to the harmonic approximation and the avoiding of crossing with the OcGr energy curve along  $e_{z1}$ .

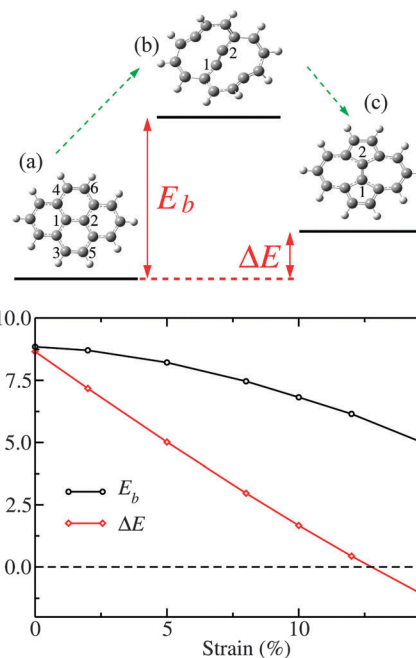


Fig. 11 The transition diagram of pyrene molecule (top), as well as the transition state energy  $E_b$  and the energy difference  $\Delta E$  of (c) from (a) as a function of uniaxial strain (bottom).

The obtained strain values for the crossing points are extreme, however, they are substantially lower than the experimentally measured value of  $\varepsilon_u = 0.25$ , corresponding to the UTS for graphene.<sup>43</sup> The directions that crossing points are found are those that the rotating bonds turn into or minimize their angle with, when the corresponding SWTs take place which result in an elongation of the lattice parameter in these directions, as a stress reduction mechanism. Indeed, given that the Young's moduli of graphene and the pentaheptites do not differ dramatically, the existence of crossing points is mostly the result of the enlargement of the equilibrium lattice parameters for the allotropes compared with graphene in these directions.

Even if they lead to energetically favored structures, SWTs can only take place if the energy barriers separating the structures are small to overcome. At ambient strain the barrier (7–9 eV) is rather prohibitive.<sup>6,37</sup> In order to estimate the dependence of the energy barrier of SWTs on the strain, we performed transition-state calculations on a strained pyrene molecule, shown in Fig. 11 (top) (a), using the Gaussian 09 program<sup>55</sup> with the B3LYP functional<sup>56,57</sup> and the 6-31G\* basis set. The strain was applied by freezing the distances between atoms 3,4 and 5,6 (Fig. 11 top panel, (a)) while the geometry of the transition state (b) was optimized. In Fig. 11 (bottom), we see that the energy difference  $\Delta E$  of the structure with SWT is reduced with strain and become energetically favorable for a strain  $\sim 12\%$  in consistency with our periodic DFT calculations. In addition, the energy barrier,  $E_b$ , for the SWT is reduced substantially from  $\sim 8.5$  eV to less than 5 eV for large strains in agreement with atomistic simulations.<sup>40</sup> Despite its substantial reduction this barrier remains large enough and prohibitive for SWTs. However, due to this substantial reduction, strain may become a possible assisting factor for the synthesis of these allotropes in the future.

## 4 Conclusions

Performing *ab initio* DFT calculations, we study the response of representative periodic graphene allotropes (namely two pentaheptites and octagraphene) to uniaxial strain for several high symmetry strain directions in comparison with graphene. Those graphene allotropes can be derived from graphene upon periodically arranged SWTs. Based on this, we study strain as a possible assisting factor for SWTs, which could make possible the synthesis of these structures from graphene.

According to our findings, pentaheptites are quite isotropic in terms of strength and Poisson's ratio, while octagraphene is not. The allotropes of our study exhibit high Young's modulus, speed of sound and UTS values, which are comparable to graphene, although smaller. Poisson's ratio is higher in pentaheptites than in graphene. For octagraphene strained along the square-diagonal direction it is similar to graphene, and for the square-edge direction it is much higher. For strain values higher than the corresponding to the UTS, the structures of our study either dissociate to linear chains, or they undergo phase transition to structures containing carbyne units.

Not all strain directions favor the conversion of graphene under strain to PeHe-A, PeHe-B and OcGr along the proposed conversion paths through SWTs. Using a model based on the harmonic approximation we determined those strain directions. In addition, using DFT calculations, we found that for tensile strains exceeding in value 12% and 10% for zig-zag and arm-chair directions, respectively, the collective SWTs shown in Fig. 1, leading to PeHe-A and PeHe-B are favored energetically. The minimal strain values obtained with the harmonic approximation model for the energy stability of the allotropes was found in the range of 9–13% for several strain directions. Although extreme, these values of strain are still smaller than the experimentally identified strain of 25% corresponding to the UTS of graphene. The energy barrier upon strain for the transition to these allotropes remains quite prohibitive, however, it is reduced significantly from 7–9 eV to 4–5 eV, allowing the possibility that strain could become an assisting factor for their synthesis from graphene, in combination with other processes like, for instance, catalysis or irradiation. However, even under high strain, it is impossible to overcome such a high energy barrier solely thermodynamically.

## Acknowledgements

NNL acknowledges support from the Thales Project GRAPHE-NECOMP, financed by the EU (ESF) and the Hellenic Ministry of Education (through ΕΣΠΙΑ) and from the GSRT action ΚΡΗΠΙΣ, project "New multifunctional Nanostructured Materials and Devices - POLYNANO". ZGF acknowledges financial support from the National Science Foundation Cooperative Agreement No. EEC-0832785, titled "NSEC: Center for High-rate Nanomanufacturing".

## References

- 1 K. S. Novoselov, D. Jiang, F. Schedin, T. J. Booth, V. V. Khotkevich, S. V. Morozov and A. K. Geim, *Proc. Natl. Acad. Sci. U. S. A.*, 2005, **102**, 10451–10453.

- 2 D. Pacilé, J. C. Meyer, C. O. Girit and A. Zettl, *Appl. Phys. Lett.*, 2008, **92**, 133107.
- 3 Y. Lin and J. W. Connell, *Nanoscale*, 2012, **4**, 6908.
- 4 Q. H. Wang, K. Kalantar-Zadeh, A. Kis, J. N. Coleman and M. S. Strano, *Nat. Nanotechnol.*, 2012, **7**, 699.
- 5 A. N. Enyashin and A. L. Ivanovskii, *Phys. Status Solidi B*, 2011, **248**, 1879.
- 6 V. H. Crespi, L. X. Benedict, M. L. Cohen and S. G. Louie, *Phys. Rev. B: Condens. Matter Mater. Phys.*, 1996, **53**, R13303–R13305.
- 7 M. T. Lusk and L. D. Carr, *Phys. Rev. Lett.*, 2008, **100**, 175503.
- 8 M. T. Lusk, D. T. Wu and L. D. Carr, *Phys. Rev. B: Condens. Matter Mater. Phys.*, 2010, **81**, 155444.
- 9 X.-Q. Wang, H.-D. Li and J.-T. Wang, *Phys. Chem. Chem. Phys.*, 2013, **15**, 2024–2030.
- 10 H. Terrones, M. Terrones, E. Hernández, N. Grobert, J.-C. Charlier and P. M. Ajayan, *Phys. Rev. Lett.*, 2000, **84**, 1716–1719.
- 11 S. J. Stone and D. J. Wales, *Chem. Phys. Lett.*, 1986, **128**, 501.
- 12 P. A. Thrower, *The study of defects in graphite by transmission electron microscopy*, Marcel Dekker, New York, 1969, vol. 5, pp. 217–320.
- 13 X. Rocquefelte, G.-M. Rignanese, V. Meunier, H. Terrones, M. Terrones and J.-C. Charlier, *Nano Lett.*, 2004, **4**, 805–810.
- 14 X.-L. Sheng, H.-J. Cui, F. Ye, Q.-B. Yan, Q.-R. Zheng and G. Su, *J. Appl. Phys.*, 2012, **112**, 074315.
- 15 Y. Liu, G. Wang, Q. Huang, L. Guo and X. Chen, *Phys. Rev. Lett.*, 2012, **108**, 225505.
- 16 H. Q. Huang, Y. C. Li, Z. R. Liu, J. Wu and W. H. Duan, *Phys. Rev. Lett.*, 2012, **109**, 269601.
- 17 H. Huang, Y. Li, Z. Liu, J. Wu and W. Duan, *Phys. Rev. Lett.*, 2013, **110**, 029603.
- 18 Y. Liu, G. Wang, Q. Huang, L. Guo and X. Chen, *Phys. Rev. Lett.*, 2013, **110**, 029602.
- 19 Y. Liu, G. Wang, Q. Huang, L. Guo and X. Chen, *Phys. Rev. Lett.*, 2013, **110**, 269604.
- 20 G. Mpourmpakis, G. E. Froudakis and E. Tylianakis, *Appl. Phys. Lett.*, 2006, **89**, 233125.
- 21 S. Lisenkov, A. N. Andriotis, I. Ponomareva and M. Menon, *Phys. Rev. B: Condens. Matter Mater. Phys.*, 2005, **72**, 113401.
- 22 Z. G. Fthenakis, Z. Zhu and D. Tománek, *Phys. Rev. B: Condens. Matter Mater. Phys.*, 2014, **89**, 125421.
- 23 C. Su, H. Jiang and J. Feng, *Phys. Rev. B: Condens. Matter Mater. Phys.*, 2013, **87**, 075453.
- 24 X.-Q. Wang, H.-D. Li and J.-T. Wang, *Phys. Chem. Chem. Phys.*, 2012, **14**, 11107–11111.
- 25 M. T. Lusk and L. Carr, *Carbon*, 2009, **47**, 2226–2232.
- 26 G. Brunetto, P. A. S. Autreto, L. D. Machado, B. I. Santos, R. P. B. dos Santos and D. S. Galvão, *J. Phys. Chem. C*, 2012, **116**, 12810–12813.
- 27 J. Kotakoski, A. V. Krasheninnikov, U. Kaiser and J. C. Meyer, *Phys. Rev. Lett.*, 2011, **106**, 105505.
- 28 J. Ma, D. Alfè, A. Michaelides and E. Wang, *Phys. Rev. B: Condens. Matter Mater. Phys.*, 2009, **80**, 033407.
- 29 J. C. Meyer, C. Kisielowski, R. Erni, M. D. Rossell, M. F. Crommie and A. Zettl, *Nano Lett.*, 2008, **8**, 3582–3586.
- 30 F. R. Eder, J. Kotakoski, U. Kaiser and J. C. Meyer, *Sci. Rep.*, 2014, **4**, 4060.

- 31 J. Lahiri, Y. Lin, P. Bozkurt, I. I. Oleynik and M. Batzill, *Nat. Nanotechnol.*, 2010, **5**, 326.
- 32 P. Y. Huang, C. S. Ruiz-Vargas, A. M. van der Zande, W. S. Whitney, M. P. Levendorf, J. W. Kevek, S. Garg, J. S. Alden, C. J. Hustedt, Y. Zhu, J. Park, P. L. McEuen and D. A. Muller, *Nature*, 2011, **469**, 389–392.
- 33 P. Simonis, C. Goffaux, P. Thiry, L. Biro, P. Lambin and V. Meunier, *Surf. Sci.*, 2002, **511**, 319.
- 34 E. Cockayne, G. M. Rutter, N. P. Guisinger, J. N. Crain, P. N. First and J. A. Stroscio, *Phys. Rev. B: Condens. Matter Mater. Phys.*, 2011, **83**, 195425.
- 35 J. N. B. Rodrigues, P. A. D. Goncalves, N. F. G. Rodrigues, R. M. Ribeiro, J. M. B. Lopes dos Santos and N. M. R. Peres, *Phys. Rev. B: Condens. Matter Mater. Phys.*, 2011, **84**, 155435.
- 36 R. Zan, Q. M. Ramasse, U. Bangert and K. S. Novoselov, *Nano Lett.*, 2012, **12**, 3936–3940.
- 37 L. Li, S. Reich and J. Robertson, *Phys. Rev. B: Condens. Matter Mater. Phys.*, 2005, **72**, 184109.
- 38 C. Ewels, M. Heggie and P. Briddon, *Chem. Phys. Lett.*, 2002, **351**, 178.
- 39 M. Kabir, S. Mukherjee and T. Saha-Dasgupta, *Phys. Rev. B: Condens. Matter Mater. Phys.*, 2011, **84**, 205404.
- 40 G. G. Samsonidze, G. G. Samsonidze and B. I. Yakobson, *Comput. Mater. Sci.*, 2002, **23**, 62.
- 41 J.-M. Leyssale, G. L. Vignoles and A. Villesuzanne, *J. Chem. Phys.*, 2012, **136**, 124705.
- 42 R. Andrew, R. Mapasha, A. Ukpong and N. Chetty, *Phys. Rev. B: Condens. Matter Mater. Phys.*, 2012, **85**, 125428.
- 43 C. Lee, X. Wei, J. W. Kysar and J. Hone, *Science*, 2008, **321**, 385–388.
- 44 P. Giannozzi, S. Baroni, N. Bonini, M. Calandra, R. Car, C. Cavazzoni, D. Ceresoli, G. L. Chiarotti, M. Cococcioni, I. Dabo, A. Dal Corso, S. de Gironcoli, S. Fabris, G. Fratesi, R. Gebauer, U. Gerstmann, C. Gougoussis, A. Kokalj, M. Lazzeri, L. Martin-Samos, N. Marzari, F. Mauri, R. Mazzarello, S. Paolini, A. Pasquarello, L. Paulatto, C. Sbraccia, S. Scandolo, G. Sclauzero, A. P. Seitsonen, A. Smogunov, P. Umari and R. M. Wentzcovitch, *J. Phys.: Condens. Matter*, 2009, **21**, 395502.
- 45 J. P. Perdew, K. Burke and M. Ernzerhof, *Phys. Rev. Lett.*, 1996, **77**, 3865.
- 46 A. Dal Corso, <http://www.quantum-espresso.org/wp-content/uploads/upffiles/C.pbe-rrkjus.UPF>.
- 47 A. M. Rappe, K. Rabe, E. Kaxiras and J. Joannopoulos, *Phys. Rev. B: Condens. Matter Mater. Phys.*, 1990, **41**, R1227.
- 48 F. Liu, P. Ming and J. Li, *Phys. Rev. B: Condens. Matter Mater. Phys.*, 2007, **76**, 064120.
- 49 X. Wei, B. Fragneaud, C. Marianetti and J. Kysar, *Phys. Rev. B: Condens. Matter Mater. Phys.*, 2009, **80**, 205407.
- 50 G. Kalosakas, N. N. Lathiotakis, C. Galiotis and K. Papagelis, *J. Appl. Physiol.*, 2013, **113**, 134307.
- 51 O. Frank, G. Tsoukleri, J. Parthenios, K. Papagelis, I. Riaz, R. Jalil, K. S. Novoselov and C. Galiotis, *ACS Nano*, 2010, **4**, 3131.
- 52 E. Cadelano, P. Palla, S. Giordano and L. Colombo, *Phys. Rev. Lett.*, 2009, **102**, 235502.
- 53 Q. Lu and R. Huang, *Int. J. Appl. Mech. Eng.*, 2009, **01**, 443–467.
- 54 Z. G. Fthenakis and N. N. Lathiotakis, Anisotropic mechanical properties of Octagraphene, to be published.
- 55 M. J. Frisch, G. W. Trucks, H. B. Schlegel, G. E. Scuseria, M. A. Robb, J. R. Cheeseman, G. Scalmani, V. Barone, B. Mennucci, G. A. Petersson, H. Nakatsuji, M. Caricato, X. Li, H. P. Hratchian, A. F. Izmaylov, J. Bloino, G. Zheng, J. L. Sonnenberg, M. Hada, M. Ehara, K. Toyota, R. Fukuda, J. Hasegawa, M. Ishida, T. Nakajima, Y. Honda, O. Kitao, H. Nakai, T. Vreven, J. A. Montgomery, Jr., J. E. Peralta, F. Ogliaro, M. Bearpark, J. J. Heyd, E. Brothers, K. N. Kudin, V. N. Staroverov, R. Kobayashi, J. Normand, K. Raghavachari, A. Rendell, J. C. Burant, S. S. Iyengar, J. Tomasi, M. Cossi, N. Rega, J. M. Millam, M. Klene, J. E. Knox, J. B. Cross, V. Bakken, C. Adamo, J. Jaramillo, R. Gomperts, R. E. Stratmann, O. Yazyev, A. J. Austin, R. Cammi, C. Pomelli, J. W. Ochterski, R. L. Martin, K. Morokuma, V. G. Zakrzewski, G. A. Voth, P. Salvador, J. J. Dannenberg, S. Dapprich, A. D. Daniels, Ö. Farkas, J. B. Foresman, J. V. Ortiz, J. Cioslowski and D. J. Fox, *Gaussian-09 Revision D.01*, Gaussian Inc., Wallingford CT, 2009.
- 56 A. Becke, *J. Chem. Phys.*, 1993, **98**, 5648.
- 57 P. Stephens, F. Devlin, C. Chabalowski and M. Frisch, *J. Phys. Chem.*, 1994, **98**, 11623.